Hall B Test Run : Drift Chamber Studies

D. S. Carman, B. Asavabiphop, S. Christo, G. E. Dodge, S. Dytman,
C. Hyde-Wright, A. Klein, S. Kuhn, M. D. Mestayer, R. Miskimen,
L. Qin, B. Quinn, B. A. Raue, R. A. Schumacher, K. Van Syok,
D. J. Tedeschi, R. A. Thompson, L. Weinstein, A. Yegneswaran

February 15, 1997

1 Introduction and Goals

The first electron beam was delivered to Hall B during the period from December 5 through December 14, 1996. A limited set of goals was put forth by the drift chamber group for this beam period. Nevertheless, these studies were extremely important to determine the range of beam-target luminosities that can be employed for the Hall B physics program. During the beam time our primary handle on the CLAS drift chamber performance were studies of the detector currents. Of primary importance was the correlation between these currents and the magnetic field (or supply current) of the minitorus. This normal-conducting toroidal magnet, positioned just inside of the Region I chamber, was designed to limit the ionization entering the active portion of the detector by sweeping the low energy Moller electrons back towards the beam pipe. These studies are crucial as the limiting luminosity for the Region I detector will be the limiting luminosity for the CLAS detector as a whole. This issue of determining a limiting luminosity for the Region I detector is essentially the assignment of a lifetime limit on the detector, as will be discussed in detail later. As well, the currents drawn by the outer tracking drift chambers in Regions II and III are just as important an issue to explore, but it is expected that the current draw per wire will achieve a maximum in the inner tracking chambers as they are closest to the beam pipe. As such, they are not only most sensitive to ionization from charged particles coming from the primary reaction target, but also are most sensitive to halo associated with the incident high energy, high intensity electron beam.

A secondary goal of the test run was to attempt to track charged particles from the CLAS target through the drift chambers in Regions I, II, and III. Analysis of this data as a function of momentum of the outgoing particles should allow for a much more realistic tuneup of the CLAS tracking software. However, due to problems with both the readout software and the TDC hardware interface, no useful tracking infomration from the recorded drift chamber data were acquired during the test run. These studies will have to await the next beam run in Hall B occurring in February 1997.

This document summarizes the results of the CLAS drift chamber studies from the December 1996 Hall B test run. Of primary importance is a determination of the drift chamber lifetimes in operating conditions of 10^{34} $cm^{-2}sec^{-1}$ beam-target luminosity, especially for the Region I detector. This luminosity represents a critical benchmark to achieve in routine Hall B operation with the electron beam in order to achieve sufficient statistical accuracy for the individual measurements of the physics program. The maximum luminosity that the CLAS can tolerate is an important issue since it will determine the smallest cross sections that can be explored with this detector system.

In an experimental environment of an intense, high energy electron beam, the high flux of electromagnetic particles produced in the primary reaction target is often the factor which limits the maximum luminosity that a specific experimental setup can tolerate. This is particularly true for the CLAS drift chambers, where each detector has direct sight of the production target. The main problem is the potential for a large number of background-related hits in the drift chambers which make the reconstruction of events nearly impossible. Presently the working assumption is that the software can tolerate no more than a 5% accidental occupancy in the drift chambers [1].

2 Drift Chamber Configuration

As the drift chambers for CLAS are still being installed and tested, only the 5 o'clock sectors of Regions I, II, and III were biased and read out during the test run. As the final high voltage system has not been procured by TJNAF, the chambers were powered by individual Bertan high voltage (HV) supplies located in the Hall B counting house. The Region II and III 5 o'clock sectors were each powered using nine HV channels. The HV granularity was such that each sector was divided into three sections, each consisting of $\sim$ 760 drift cells. Each section employed three HV channels, one each for the guard wires, the field wires, and the sense wires. These sections of the chamber were called the forward, intermediate, and backwards regions, respectively, from sector nose to sector tail. Each section subtended a distinct angular range and included both the axial (or inner) and stereo (or outer) superlayers. The angular range subtended by each of these sections is shown in Table 1, where Θ_{CLAS} is the polar angle with respect to the beam axis and an origin defined by the location of the solid target.

Section	Θ_{CLAS}
Fwd	$10^\circ \rightarrow 55^\circ$
Int	$55^\circ \rightarrow 100^\circ$
Bck	$100^\circ \rightarrow 145^\circ$

Table 1: Polar angle ranges subtended by each of the three portions of the Region II and Region III sectors.

The detector installed in the Region I 5 o'clock position consisted of a prototype sector described in detail elsewhere [2]. This prototype sector consisted of six individual drift cells in the axial (or inner) superlayer positioned along the endplates at representative locations to span nearly the full polar angle acceptance subtended by the Region I detector. This prototype sector also contained one fully instrumented section outfitted with a single signal translator board (STB) and high voltage translator board (HVTB). This portion of the prototype detector consisted of roughly 64 drift cells in the stereo (or outer) superlayer and roughly 96 drift cells in the axial superlayer.

The individual drift cells in the Region I prototype were labelled consecutively from sector nose to sector tail as P1 through P6. The instrumented portion of the prototype was labeled as STB8. Each individual drift cell employed a separate HV channel for the guard and field voltages with the sense wires held at ground potential. The instrumented portion of the detector employed separate HV supplies for the sense and field voltages with the guard wires held at ground potential. The angular positions of these wires are shown in the Table 2.

Cell	Θ_{CLAS}
P1	13°
P2	22°
P3	35°
P4	55°
P5	75°
P6	140°
STB8	85° $\rightarrow$ 129°

Table 2: Polar angle positions of the wires in the Region I prototype detector.

3 Gain Equalization

In order to directly compare the current draw by each of the detectors, the chamber high voltages must be set to yield the same gas gains. Gain calculations were performed employing a simple algorithm assuming a hexagonal drift cell configuration [3]. The goal in setting the chamber voltages is to equalize the gas gains for all three regions while maintaining the chamber efficiencies in the plateau regime. For the test run all three drift chambers employed an argon/CO_2 gas mixture (85% - 15% molar). However, the calculation assumed an argon/ethane gas mixture (50% - 50% molar) as this is where precisely measured gas gain data were available. For a gas gain of 7×10^4, the field-sense voltage differences for the three regions were determined to be: R1: 2300 V, R2: 2550 V, R3: 2700 V. Thus a difference between Region II and Region I of 250 V, and a difference between Region III and Region I of 150 V. These same voltage differences were carried over to the argon/CO_2 mixture using the measured Region I prototype data for the plateau voltage and gas gain for this gas mixture as our reference [2]. For a gas gain of 7×10^4, this yields the following sense-field voltage differences for the drift chambers:

R1 : 2000 V
R2 : 2250 V
R3 : 2400 V

For Regions II and III the sense to field voltages must be set in the ratio of 2 to -1. This results in the most uniform electric field configuration from drift cell to drift cell and wire layer to wire layer as indicated by GARFIELD electric field calculations [4]. For Region I, due to the design of the printed circuit boards, the sense to field voltage ratio must be set in nearly a 1 to -1 ratio. The guard voltages for Regions II and III were determined from a calculation of L. Qin of ODU for Region II [5], which provided the required guard voltage for a given sense and field voltage. Region I guard voltages for the instrumented portion of the sector (STB8) were set to ground for convenience.

Detailed efficiency and gain measurements were made for the individual drift cells and the instrumented section of the Region I prototype [2]. It was found that the voltage for the individual drift cells had to be set 200 to 300 V higher than the cells in the instrumented portion of the detector to equalize the gas gains. This voltage difference for an identical cell

geometry is most likely due to one of two effects. The first is that the isolated drift cells have less efficiency far from the sense wire due to the lack of neighboring cells. This results in a lower electric field between the field wires, and hence could affect the efficiency. Our GARFIELD [4] calculations comparing the two cases indicate that this argument may have validity at some level. The other explanation involves differences in capacitance between the isolated drift cells and the cells of the instrumented section. This difference in capacitance results as the sense wires of the isolated drift cells were connected to the STB through lengths of coaxial cable, whereas the sense wires of the instrumented section were connected directly to the STB employing conductive rubber inserts.

The final sense, field, and guard voltages employed for the drift chambers in the Hall B December test run are included in Table 3.

		V_s	V_f	V_g
Region I	Cells P1 $\rightarrow$ P6	gnd	-2200 V	-1100 V
	STB8	+800 V	-1100 V	gnd
Region II	(F,I,B)	+1500 V	-750 V	+525 V
Region III	(F,I,B)	+1600 V	-800 V	+560 V

Table 3: Drift chamber voltages employed for the Hall B test run.

Notice that our gas gain calculations for Region I had indicated an operating point such that the sense-field voltage difference should be 2000 V to achieve a gas gain of 7×10^4. However, a difference of only 1900 V was employed for STB8. This reduction was necessary to limit excessive currents within STB8 during the initial part of the Hall B test run. This 100 V reduction amounts to a reduction in gas gain of roughly a factor of three, since the gas gain depends exponentially on the applied voltage.

4 Drift Chamber VI Studies

The first of the drift chamber beam studies shown are simple VI curves for the different chambers. These data provide an indirect measurement of the chamber gas gain by plotting the chamber voltage ($\Delta V_{sense-field}$) versus the chamber current draw. The basic principle of drift chamber operation is that when charged particles pass through the drift cell and the chamber gas environment, a certain number of electron-ion pairs will be created directly along the path of the particle. The mean number of ion pairs created is directly proportional to the energy deposited in the drift cell. Under the action of an applied electric field, the electrons are accelerated towards the sense wire, and the positively charged ions are accelerated towards the field wires. The current measured at the high voltage supplies, however, depends on the electric field intensity. At zero voltage no charge is collected as the electron-ion pairs recombine under their own electrical attraction. As the voltage is increased, however, the recombination forces are overcome and the current measured begins to increase as more and more of the electron-ion pairs are collected before they can recombine. At some

point all created ion pairs are collected and further increases in voltage will show no effect. This mode of operation results in essentially unity gain of the detector.

If the voltage is further increased beyond the unity gain region, the current again begins to increase with voltage. At this point, the electric field is strong enough to accelerate freed electrons to an energy where they are also capable of ionizing gas molecules near the sense wire. Electrons liberated in these secondary ionizations are also accelerated to produce still more ionization and so on. This results in what is known as an ionization avalanche about the sense wire. The number of electron-ion pairs created in the avalanche, however, remains directly proportional to the number of primary electrons created along the path of the incident charged particle. What results then is a proportional amplification of the chamber current with a gain factor depending on the applied voltage. This is the so-called proportional region of the chambers, and represents the desired operational mode. The desired gas gain for all chambers has been chosen to be $\sim 7\times10^4$.

If the chamber voltage is increased still further, beyond gains of $\sim10^6$, the total amount of ionization created through multiplication becomes sufficiently large that space charge effects distort the electric field near the sense wire and proportionality begins to be lost. At still higher voltages, the energy becomes so large that electrical discharge occurs in the gas. These last two modes of operation are to be avoided as they result in poor performance of the detector, and can also damage the chamber either through pitting of the small diameter sense wires (20μm gold-plated tungsten) or hydrocarbon deposits in the chamber which can act as breakdown paths.

The VI data for Region I is shown in Fig. 1 and that for Regions II and III is shown in Fig. 2. All data were acquired with a 75 nA CW electron beam. For Regions II and III and the instrumented portion of Region I, the field and guard voltages were held fixed while the sense voltage was varied. For the individual drift cells of Region I, the sense and guard voltages were held fixed while the field voltages were varied.

The VI curves in Fig.1 for the individual drift cells clearly show the transition from the unity gain region of operation to the proportional mode. Once in the proportional mode of operation, the current (and hence the gain) increases exponentially with applied voltage over several orders of magnitude, as expected. The VI curves for Regions II and III are shown in Fig. 2 for the forward, intermediate, and backwards portions of the detectors. Again the current increases exponentially with applied voltage over several orders of magnitude. We do notice, however, that the current draw tends to be larger for the more forward regions of the detector. This comes from the more forward portions of Regions II and III having a larger incident beam-related flux through them than the backwards regions of the detector. This larger ionization results in a higher current draw due to the larger number of ion pairs within these more forward cells. We should expect identical VI curves for the forward, intermediate, and backwards portions of Regions II and III only in the idealized situation of a perfectly uniform distribution of ionization through the chambers.

5 Region I Beam Studies

This section reports on the current measurements in Region I varying the minitorus current with the main torus magnetic field on and off. These current studies were performed

with both CW and pulsed electron beams. The beam-target luminosities employed were 8.4×10^{32} cm^{-2}sec^{-1} for the CW beam and 8.3×10^{33} cm^{-2}sec^{-1} (instantaneous) for the 2% duty cycle pulsed beam. The beam energy employed for these studies was $\sim$ 2.4 GeV, and as such, the nominal operating point for the main torus was at half its nominal full field. This nominal full field is about $\int$ B $\cdot$ dl = 1.5 T $\cdot$ m. The maximum field of the minitorus is roughly 5% that of the main torus.

The minitorus is a normal-conducting toroidal magnet that is placed just inside of the Region I detector. It is designed to remove low momentum electrons from the active area of the drift chambers. GEANT simulations with and without the minitorus have been carried out by V. Burkert of TJNAF [6], and are shown in Fig. 3 and Fig. 4. These simulations were carried out assuming a beam-target luminosity of 10^{33} cm^{-2}sec^{-1}. Fig. 3 and Fig. 4 represent a picture of detector hits developed over a 200 nsec time window. With the minitorus field off, a charged particle of sufficient energy can be trapped by the main torus field thereby spiralling through the active portion of the Region I detector producing an indefinite number of hits in multiple sectors. The interpretation of the event then becomes nearly impossible to extract as these events must be disentangled from charged particles passing through the detector. The simulation carried out with the minitorus in place at full field clearly shows that almost all of the low energy Moller electrons are contained well inside the radius of the Region I detector close to the beam pipe. Thus as shown in Fig. 4, significant drops should be expected in the measured Region I currents with the minitorus magnetic field present.

The experimental data for Region I are displayed in Fig. 5, Fig. 6, and Fig. 7. Each figure shows the measured currents for the individual drift cells and the instrumented section on different plots. This was done to avoid confusion in the direct comparison of the data as the individual cells and STB8 were operated at different gas gains. It is estimated that the gas gain for the cells in STB8 is about a factor of three lower than that for the individual drift cells.

Fig. 5 and Fig. 6 show the measured Region I currents employing a 75 nA CW beam on a 3 mg/cm^2 carbon target (target wheel position at $\Theta = 111^\circ$). This represents a beam-target luminosity of 8.4×10^{32} cm^{-2}sec^{-1}. The upper half of Fig. 5 and Fig. 6 show the measured leakage current in the individual drift cells (in nA) as a function of Θ_{CLAS} (in degrees) for minitorus currents in the range from 0 to 2 kA, or about one fourth of its nominal full field. Each curve represents a different setting of the minitorus field. The currents measured in the individual drift cells are given by reading off the data points at a constant value of Θ_{CLAS}. The difference between the data in Fig. 5 and Fig. 6 was that the main torus was off for the former data set and set to half of its maximum field ($\sim$ 1900 A) for the latter data set. In either case, the currents in the Region I detector reach a maximum at roughly $\Theta_{CLAS} = 60^\circ$. As the minitorus current is increased, the chamber current drops from a maximum value of 450 nA at zero current to less than 20 nA at 2 kA minitorus current. At minitorus currents of greater than $\sim$ 2 kA, the angular dependence of the background ionization is apparently eliminated. However, what is effectively happening to the low energy background can be seen more clearly by taking into account the current per centimeter of wire. At zero minitorus field the background is seen to be much more uniform if we take into account the different lengths of the sense wires in going from cell P1 to P6. These wire lengths are estimated in Table 4.

As the minitorus field is increased, the low energy background is swept forward and bent

Cell	Wire Length (cm)
P1	10
P2	26
P3	40
P4	49
P5	55
P6	56
STB8	56

Table 4: Estiminate Region I prototype wire lengths.

back towards the beam pipe. As the minitorus current is increased from 0 to 2 kA, we can clearly see this redistribution. Fig. 8 shows this effect by simply redisplaying Fig. 5, through Fig. 7 for the individual drift cells P1 through P6 dividing out the different wire lengths using the measurements in Table 4.

The bottom half of Fig. 5 and Fig. 6 show the measured leakage currents in STB8 as a function of minitorus current. If the gain difference between STB8 and the individual drift cells is taken into account, it is seen that the measured currents in STB8 are reasonably consistent with those in the individual drift cells, at least to within a factor of two. This comparison is made by dividing the measured STB8 currents by 160 (the number of cells in STB8) and multiplying by 3 (the expected gain difference). This comparison is fairly crude as the assumed distribution of currents as a function of Θ_{CLAS} using cells P1 $\rightarrow$ P6 is only a rough approximation for STB8 due to the large gap between P5 (at $\Theta_{CLAS} = 75°$) and P6 (at $\Theta_{CLAS} = 140°$).

Note that the currents measured in STB8 as a function of minitorus current fall off quite rapidly in going from 0 to 1 kA, and then remain essentially flat as the current in the minitorus is increased still further. This is extremely encouraging with regards to both Region I operation and minitorus operation. From the standpoint of minitorus operation, the power supply has a maximum output current of 8000A. It is extremely encouraging that the majority of the excess current draw in Region I is removed at only $\sim 1/4$ of the maximum current, and thus the power supply can be operated in a much safer regime. This also implies that the maximum temperatures in the coils of the minitorus itself remain in a much more limited range at the lower minitorus supply currents (T $\approx 80° \rightarrow 130°$ F). From the standpoint of Region I operation this is good news as there were concerns that excessive heat from the magnet could not only overheat the on-chamber preamplifiers, but also possibly damage the 1 mil aluminized nylon gas windows.

Shown in Fig. 7 are the same sort of plots shown in Fig. 5 and Fig. 6 except with a pulsed beam (2% duty cycle) with an average current of 24 nA on a 100 μg/cm^2 BeO target ($\rho =$ 3.1 gm/cm^3, target wheel position at $\Theta = 169.5°$). This corresponds to an instantaneous beam-target luminosity of 8.3×10^{33} cm^{-2}sec^{-1}. There is an apparently similar distribution of currents in the individual drift cells and a much larger current draw in STB8 compared to the same data with the CW electron beam. However, upon closer inspection it is seen that although the peak currents in the individual drift cells are about the same near $\Theta_{CLAS} \sim$

60° with the minitorus field off, the distribution is clearly more backwards-peaked in Region I. This indicates a different beam-related background in Region I with the pulsed beam compared to the CW beam for these specific tunes.

The pulsed beam data clearly show that this pulsed beam tune was much worse than this CW beam tune. This can be seen in the individual drift cells with currents of nearly 60 nA even at minitorus currents of 5 kA. As well, the currents in STB8 are nearly an order of magnitude larger with the pulsed beam compared to the CW beam with the minitorus off. These comparative data are in accord with the on-line rates seen in the electromagnetic calorimeters and forward angle TOF detectors on the forward carriage. These detectors also saw much larger background with the pulsed beam compared to the CW beam. This background difference arises due to the fact that the lower CW beam currents employed by Hall B are controlled by a chopper system, whereas the lower pulsed beam currents are set by closing down a pair of beam line slits at the entrance to the experimental hall which leads directly to slit edge scattering background.

Note again that the results of the current measurements in STB8 with the pulsed beam in Fig. 7 are reasonably consistent with those measured for the individual drift cells provided the difference in gains is taken into account. Again agreement in terms of current per wire is within a factor of two presuming that the interpolation of currents from P5 and P6 to the angular range subtended by STB8 is accurate.

The data shown in Fig. 5, Fig. 6, and Fig. 7 have all been corrected for non-target-related background. Several data points were compared (0, 3 kA minitorus current) with and without a target in the beam. The target out measurements were subtracted from the target in measurements to yield only the target-related currents. This procedure was adopted before attempting any extrapolation to luminosities of 10^{34} $cm^{-2}sec^{-1}$ because it is believed that with sufficient operational experience and beam tuning diagnostics, the majority of the non-target related background can be eliminated. However, as target out measurements were made at only two different minitorus currents, the subtraction procedure employed must be explained. The procedure adopted was to compare the chamber currents at 0 and 3 kA minitorus current with and without the target. It was found that the ratio between the target in and target out chamber currents was nearly a constant fraction for each individual Region I drift cell and STB8 at the two minitorus currents studied. With this result, this same reduction factor found for each drift cell and STB8 was employed at all minitorus currents.

6 Region I Lifetime Predictions

Problems that limit the useful lifetime of wire chambers are known as aging effects. Typical symptoms of aging include loss of gas gain, reduction or shortening of the efficiency plateau, loss of timing resolution, excessive leakage currents, self-sustained current discharge, and sparking. In general terms, the main symptoms related to wire chamber aging fall into one of two categories: (1) loss of gain or loss of gain uniformity with applied voltage, or (2) electrical breakdown usually manifested by a self-sustaining dark current discharge (where dark current is a current not induced by a radiation source) [7]. The effects of gain problems are usually attributed to a polymer build-up or coating on the sense wires, while breakdown

problems are usually attributed to a polymer coating on the field wires. Wire chambers have shown serious aging symptoms with accumulated charges of less than 0.01 coulombs per centimeter of wire. However, there are also many examples of wire chambers that have been operated with little or no deterioration in performance even after being exposed to relatively high radiation levels for long periods of time.

The useful lifetime of a chamber is a very difficult quantity to specifically define as it depends on many different parameters such as construction materials, purity of the operating gas, chamber geometry, and other still unknown effects. However, for the purposes of this document the useful chamber lifetime is defined assuming an amount of charge collected per centimeter of wire of 1.0 coulomb. Again, this may be an underestimate or overestimate of the true chamber lifetime.

In order to extract the expected lifetime of the Region I detector, it is necessary to scale the results obtained for the Region I prototype detector to the expected CLAS operating luminosity of 10^{34} cm^{-2}sec^{-1}. The lifetime definition (in years) is given by:

$$\text{Lifetime} \;=\; (1\ \text{coul/cm}) \cdot \frac{l_w(\text{cm})}{\langle i_s \rangle (\text{coul/sec})} \cdot (3.15 \times 10^7 \text{sec/year})^{-1} \qquad (1)$$

In this expression, l_w is the length of the wire and $\langle i_s \rangle$ is the chamber current extrapolated from the data at a luminosity of 8.4×10^{32} cm^{-2}sec^{-1} to a luminosity of 10^{34} cm^{-2}sec^{-1}.

Fig. 9 shows the extrapolated lifetime for the Region I prototype detector for the individual drift cells P2 through P5 and STB8 as a function of minitorus current. This calculation employed the data in Fig. 6 as a starting point for the extrapolation with a CW beam with the main torus on at half field for a 2.4 GeV electron beam. The dashed curves represent the predicted chamber lifetimes employing the target out subtraction, while the solid curves do not employ the target out subtraction. In this manner we arrive at a range of predicted lifetimes (the region between the two curves). The dashed line represents a more idealized situation with no target out related background present, or in other words an extremely clean beam tune. The solid line represents a possibly more realistic scenario with a halo accompanying the beam that is also responsible for part of the measured currents in the chamber.

It should also be noted that the rapid rise in the lifetimes of the individual drift cells about 2 kA minitorus current may be an unphysical effect brought about by the 5 nA minimum current resolution on the Bertan HV supplies employed. This may give rise to inaccurate current measurements below 10 nA on the supplies. However these results indicate typical Region I lifetimes of at least 5 years at a luminosity of 10^{34} cm^{-2}sec^{-1} at or above minitorus currents of 2 kA. As well, due to the lower gains employed for the instrumented portion of the Region I prototype, expected lifetimes for these wires are correspondingly higher.

One important point to make at this time regards the target employed for these beam studies. It was initially throught during the test run that the measurements were made employing a 1 mg/cm^2 carbon target. After the run was completed a survey measurement revealed that the measurements were most likely made with a 3 mg/cm^2 carbon target. This leads directly to a factor of three change in the predicted chamber lifetimes. The final answer to this question will have to await further measurements in the drift chambers in February 1997.

7 Region II and Region III Beam Studies

The results of the test run beam studies for the Region II and Region III detectors again take the form of measured chamber currents as a function of minitorus current. The data for the forward, intermediate, and backwards portions of these detectors are shown in Fig. 10 and Fig. 11. The beam conditions for the data in these figures are identical to that for the Region I data in Fig. 5 and Fig. 6. The data, which were acquired simultaneously for all of the drift chambers, employed a 75 nA CW electron beam on a 1 mg/cm^2 carbon target yielding a beam-target luminosity of 8.4×10^{32} cm^{-2}sec^{-1}. For Fig. 10, the chamber current data was acquired with the main torus field off, and the data in Fig. 11 was acquired with the main torus on at half field ($\sim$ 1900 A). Again the data are shown with the target out background currents subtracted using the same procedure that was described for the Region I data analysis.

It is interesting how much of an effect the minitorus has on the chamber currents in the Region II and III chambers with the main torus field off. Current drops of roughly an order of magnitude were seen in going from a minitorus current of 0 to 2 kA. This result was even more suprising at the time of the measurement as the main torus control program had indicated that the magnet was set to 1900 A. However it was found that this control program had crashed and the magnet was actually off. Simulations have indicated that with the main torus powered up, the minitorus should have a relatively minor effect on the Region II currents, and nearly no effect on the Region III currents.

After the main torus field was found to be off, the measurements of the chamber currents versus minitorus current in Regions II and III were repeated with the main torus field set to half of its nominal full field value. Results much more in agreement with expectations were seen, namely that the currents in Regions II and III remained essentially flat with minitorus current as shown in Fig. 11. The slight increase in chamber currents witnessed at the higher minitorus currents may be due to a change in the beam tune over the 30 minutes that the data sample was acquired.

One issue that remains a concern from these measurements regards the elevated chamber currents in the forward portion of the Region III sector. However we believe that we are seeing background from high energy electrons that are passing through the downstream opening of the cryostat (around the beam pipe). In this reversed magnetic field region, these electrons from the target or beam halo can be bent back around into the forward part of Region III. In the normal CLAS operating configuration, the forward carriage is positioned up against the downstream end of the cryostat. The forward carriage contains a two inch thick lead shield that surrounds the beam pipe and is designed to stop these low electrons so that they do not provide an additional background to the detectors on the forward carriage or the drift chambers. However, for this test run the forward carriage was positioned approximately 2 m downstream of its nominal position, allowing the high energy background to pass through. The final answer to this puzzle will have to await the next Hall B beam period in February 1997.

Due to the fact that the shielding configuration for this test run was less than optimal and most likely resulted in higher leakage currents in Region III and possibly Region II, lifetime estimates were not made for these detectors. However, even for the leakage currents recorded, the extrapolated lifetime at a luminosity of 10^{34} cm^{-2}sec^{-1} of the shortest Region

II wire is expected to be over 50 years, and the lifetime of the shortest Region III wire is expected to be over 10 years.

8 Summary and Conclusions

The primary results of the December test run for the drift chambers are the estimated lifetimes of the Region I detector at an operating luminosity of 10^{34} $cm^{-2}sec^{-1}$. As stated, the limiting luminosity (defined as lifetime) for the Region I detector represents the limiting luminosity for the CLAS detector as a whole. Our results indicate a lifetime for the Region I detector at luminosities of 10^{34} $cm^{-2}sec^{-1}$ on the order of 5 years at a minitorus current setting of 2 kA and a carbon target. In other words, it will take roughly 5 years for the wires of the Region I detector to accumulate 1 coulomb of charge per centimeter. This prediction is in accord with our pre-run expectations. However, one might argue that a 5 year useful lifetime of a chamber that took nearly 10 years to design and construct is a particularly short return on such a large and costly investment. Given this point of view there are several remarks that must be made:

1). The lifetime estimate of 5 years does not represent a physical 5 year period due to the fact that Hall B will never be in full year-round operation, but is expected to run only a part of the time in any given calendar year. Furthermore, CLAS will only operate at luminosities of 10^{34} $cm^{-2}sec^{-1}$ during part of the electron beam portion of its program. During real photon running, maximum achieveable luminosities are not expected to be above 10^{33} $cm^{-2}sec^{-1}$. As well, with a real photon beam there are not contributions from Moller electrons. Accounting for this, it may be the case that the drift chambers could operate for as long as 10 years before the onset of any noticeable aging effects.

2). One of the important design features of the CLAS project is that many different experiments will acquire data concurrently. In this way the 'physics payoff' per unit of time is much greater than for an experimental facility where only one reaction or state can be studied during a given beam period.

3). Finally the definition of lifetime really only assumes the length of time that a chamber can be operated without maintenance attention. If a portion or portions of the chamber begin to show signs of aging, there are several actions that can be undertaken to increase the detector lifetime. These include backfiring (or reversed-bias operation) and cleaning of the wires, although these techniques may or may not have a beneficial effect depending on the nature of the problem.

4). Our lifetime predictions result from data collected with a carbon target. The majority of CLAS running however will employ low A targets such as hydrogen and deuterium. This will tend to increase the lifetime estimates due the the reduced electromagnetic background.

One additional feature in our favor for the Region I detectors that has not been discussed to this point in time regards the addition of a small amount of alcohol to the chamber gas mixture. Alcohol in quantities of less than 5% by volume of chamber gas has been shown to dramatically increase the useful lifetime of a chamber. Alcohol is a non-polymerizing

additive which has an ionization potential energy lower than any other component in the gas mixture. The addition of an agent such as methylal or propylic alcohol changes the molecular ions at the field wires into a non-polymerizing species through ion-exchange. The addition of alcohol is expected to substantially increase the integral flux capability of a proportional-type chamber [8]. Although not used for the Region I prototype detector, alcohol will be added to the gas mixture for normal Region I detector operation. How this will ultimately affect the lifetime of the Region I detector remains an issue of interest.

The bottom line is that early beam studies with the CLAS drift chambers are quite promising with no major suprises to this point. However there is still much work to be accomplished before the next running period, and still much more to be learned about the operation of the drift chambers in the harsh environment of the experimental hall.

References

[1] M. Mestayer, TJNAF, private communication.

[2] D. S. Carman, *"CLAS Region I Prototype Detector"*, CLAS-note 96-022, (1996).

[3] M. Mestayer, *"Calculation of Drift Chamber Gas Gain"*, CLAS-note 96-005, (1996).

[4] GARFIELD has been developed at the University of Mainz by R. Veenhof and revised by M. Guckes and K. Peters. See HELIOS note 154 (1986).

[5] L. Qin, *"Region II Drift Chamber"*. This notebook contains detailed information pertaining to sector instrumentation.

[6] V. Burkert, TJNAF.

[7] J. A. Kadyk, Nucl. Inst. Methods A300, 436(1991).

[8] F. Sauli, *"Principles of Operation of Multiwire Proportional and Drift Chambers"*, CERN Report 77-09, (1977).

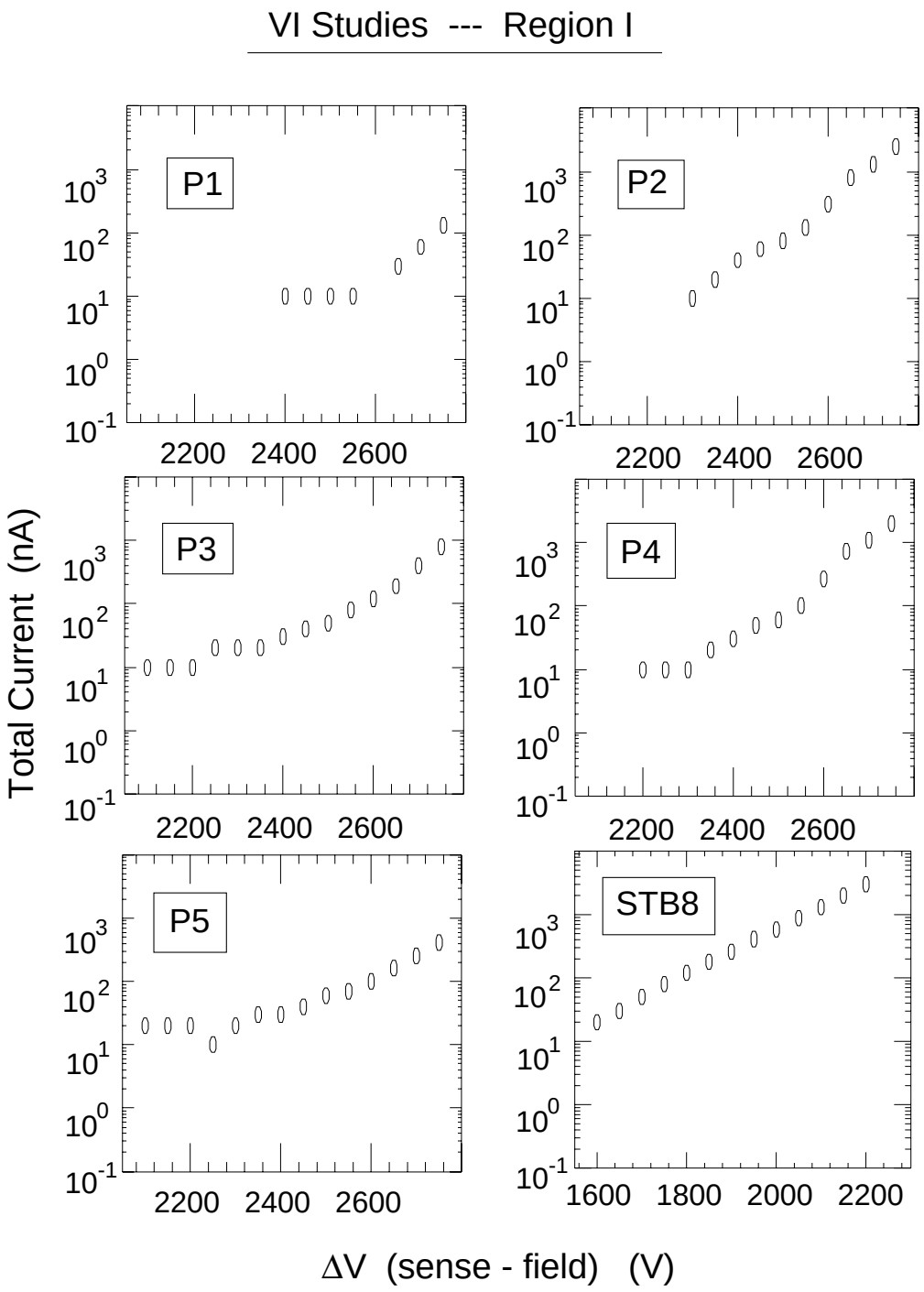

Figure 1: Region I measured leakage currents as a function of the voltage difference between the sense and field wires recorded at a constant beam current for the drift cells P1 through P5 and STB8.

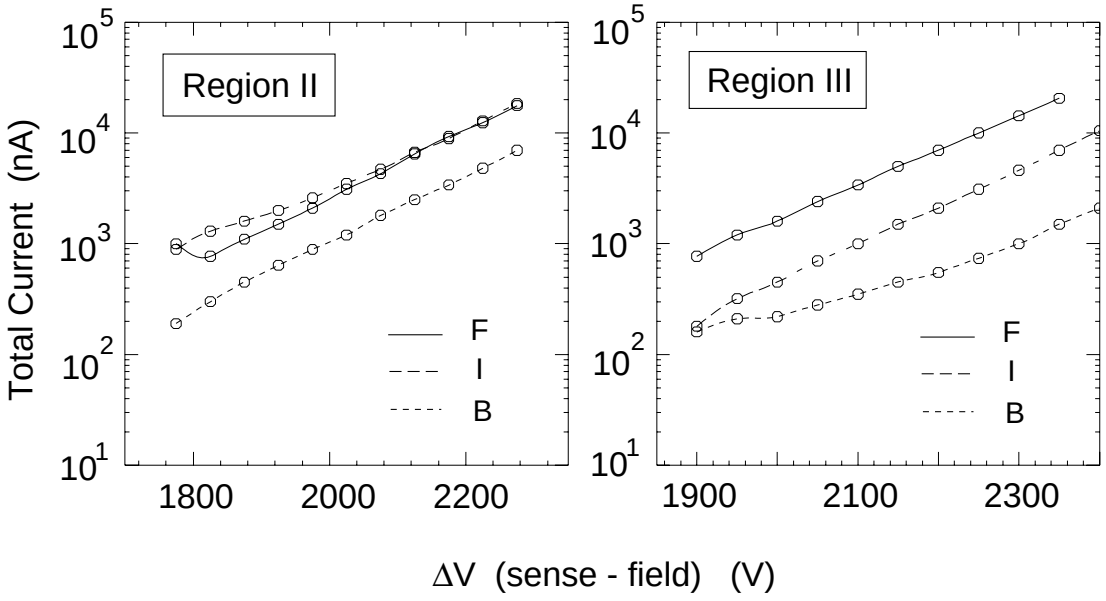

Figure 2: Region II and Region III measured leakage currents as a function of the voltage difference betweeen the sense and field wires recorded at a constant beam current. The three separate curves in each figure denote the forward, intermediate, and backwards portion of each detector.

Figure 3: GEANT Monte Carlo simulation of the background present in the Region I detector with the main torus field on and the minitorus field off. The simulation shows a snapshot taken over a 200 nsec time window with a beam-target luminosity of 10^{33} cm^{-2}sec^{-1} assuming an incident electron beam.

Figure 4: GEANT Monte Carlo simulation of the background present in the Region I detector with the main torus field and the minitorus field on. The simulation represents a snapshot taken over a 200 nsec time window with a beam-target luminosity of 10^{33} cm^{-2}sec^{-1} assuming an incident electron beam.

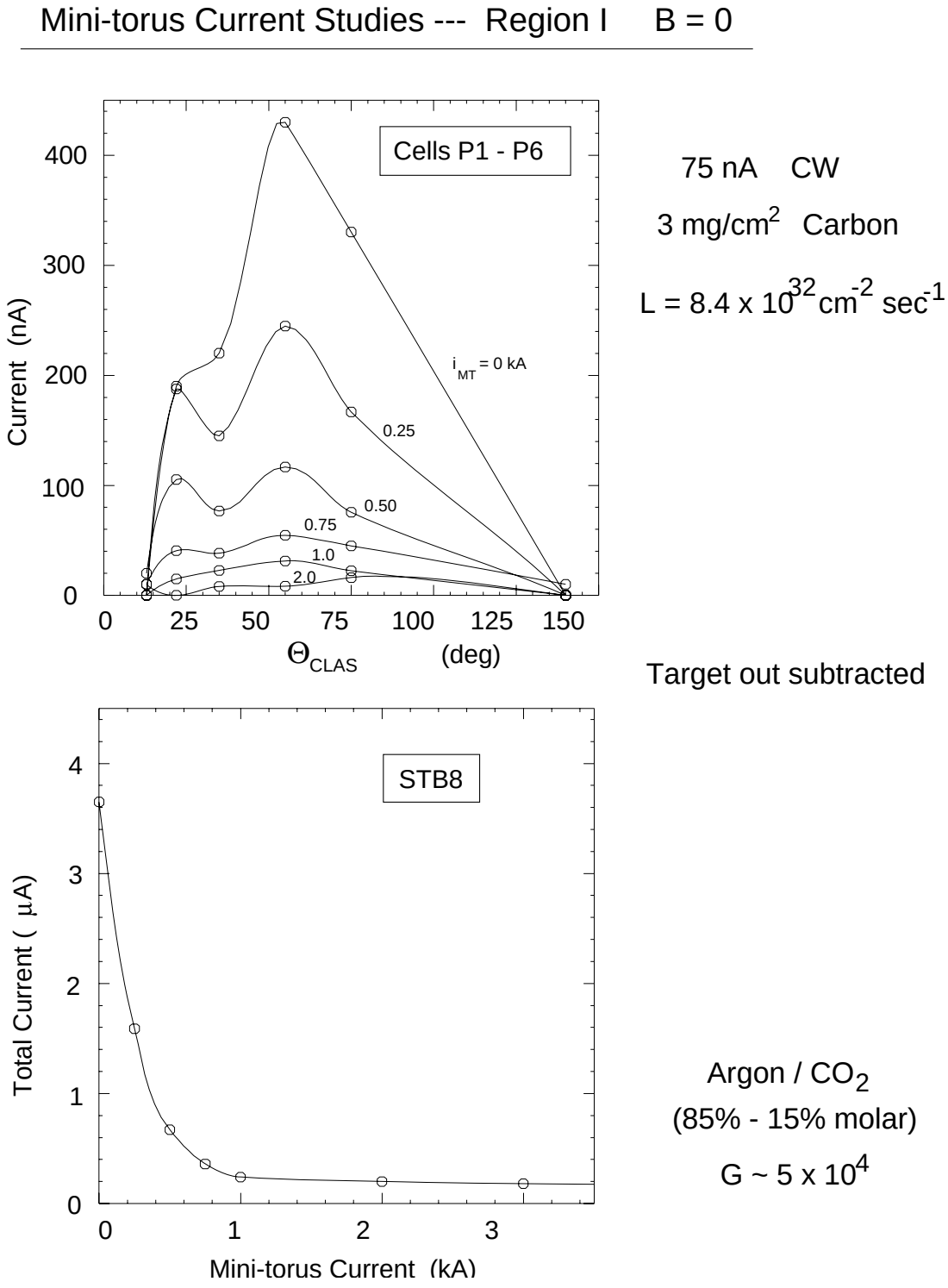

Figure 5: Top: Region I data for the individual drift cells plotting the measured leakage current vs. Θ_{CLAS} for a range of minitorus currents from 0 to 2 kA. Bottom: Region I data for STB8 plotting the total measured leakage current vs. minitorus current from 0 to 3 kA. This data was acquired with a 75 nA CW electron beam on a 3 mg/cm^2 carbon target with the main torus field off. The gas mixture and operating conditions of the chamber can be found in the text.

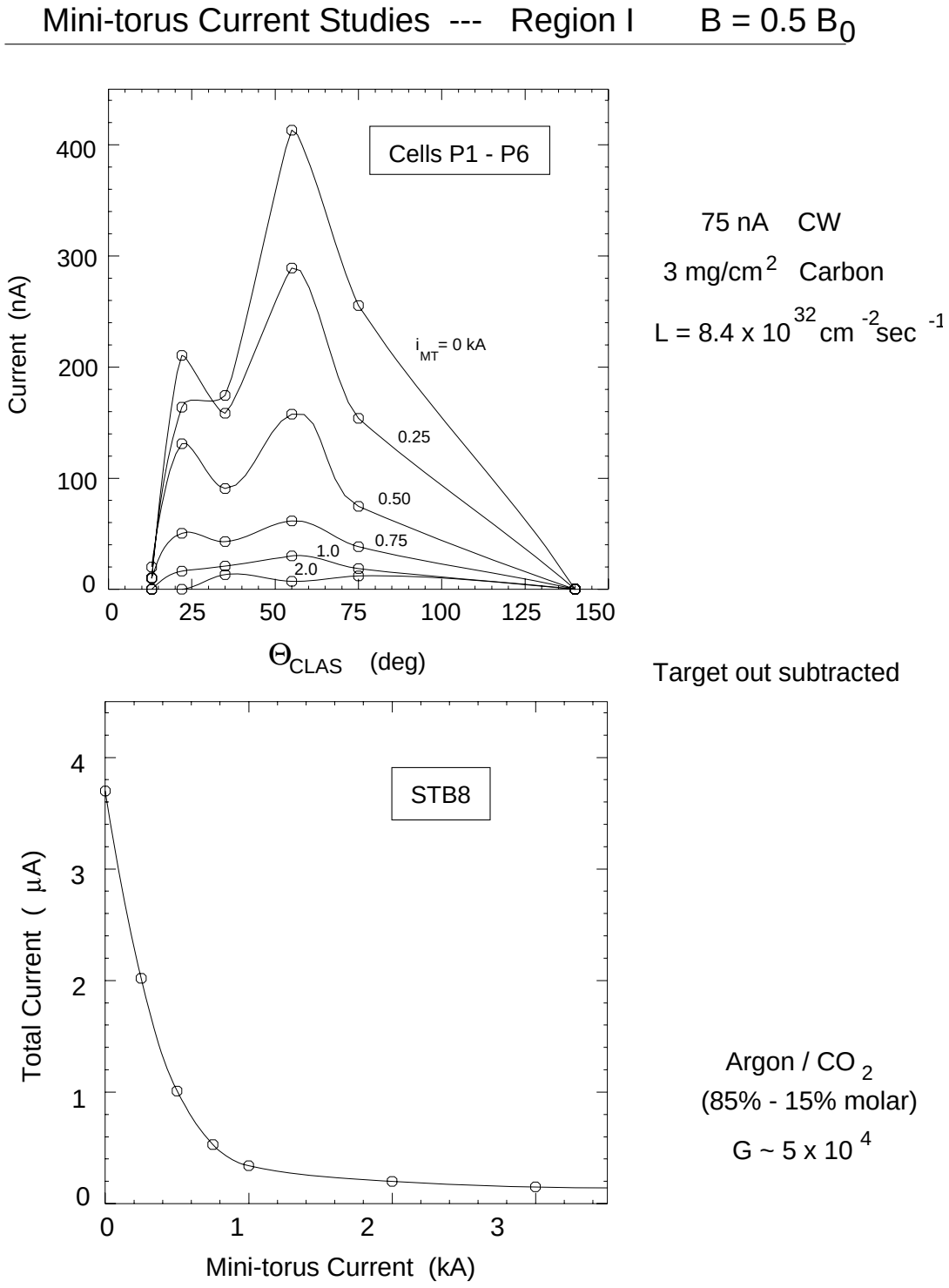

Figure 6: Top: Region I data for the individual drift cells plotting the measured leakage current vs. Θ_{CLAS} for a range of minitorus currents from 0 to 2 kA. Bottom: Region I data for STB8 plotting the total measured leakage current vs. minitorus current from 0 to 3 kA. This data was acquired with a 75 nA CW electron beam on a 3 mg/cm^2 carbon target with the main torus on at half field. The gas mixture and operating conditions of the chamber can be found in the text.

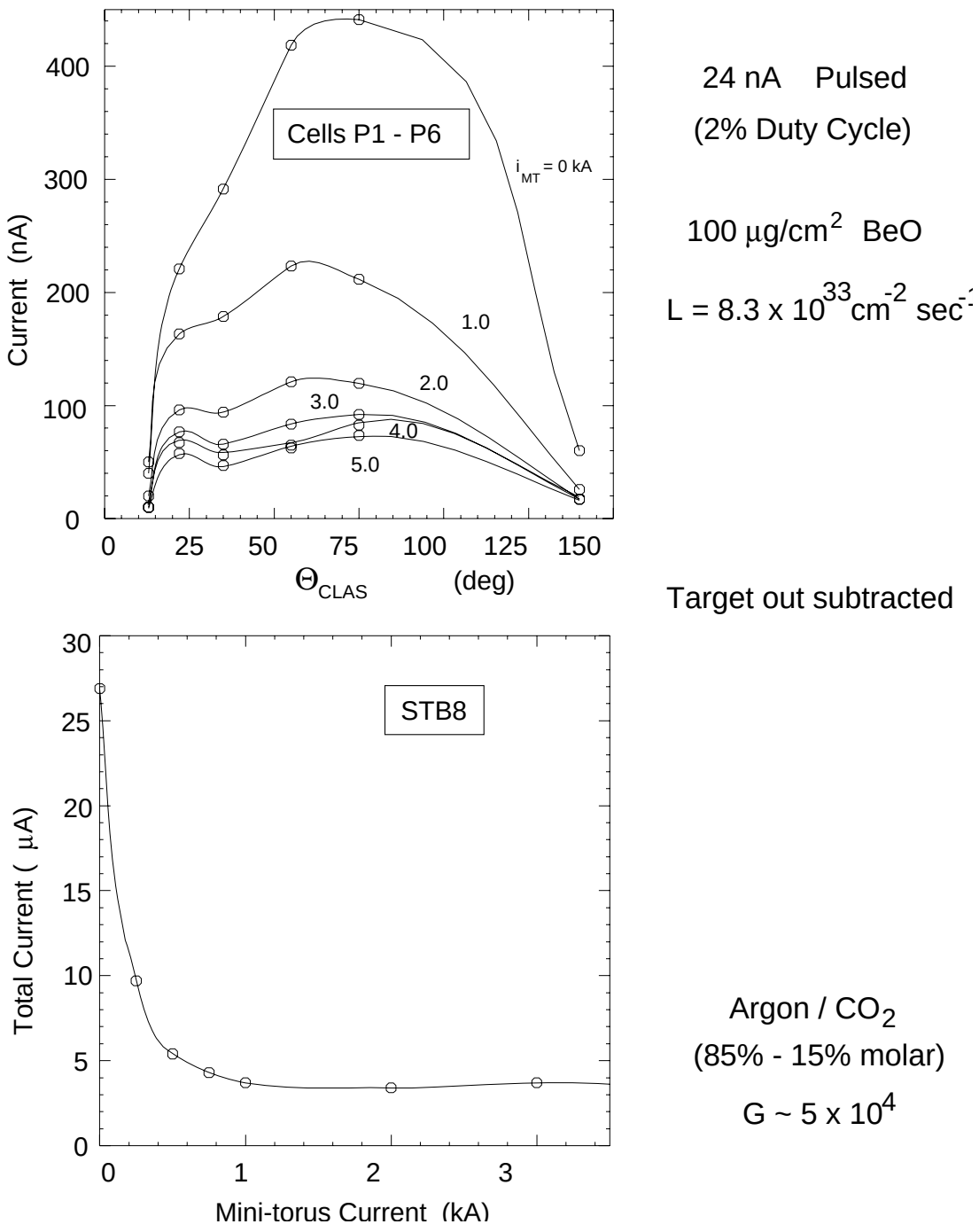

Figure 7: Top: Region I data for the individual drift cells plotting the measured leakage current vs. Θ_{CLAS} for a range of minitorus currents from 0 to 5 kA. Bottom: Region I data for STB8 plotting the total measured leakage current vs. minitorus current from 0 to 3 kA. This data was acquired with a 24 nA (average) pulsed electron beam on a 3 mg/cm^2 carbon target with the main torus on at half field. The gas mixture and operating conditions of the chamber can be found in the text.

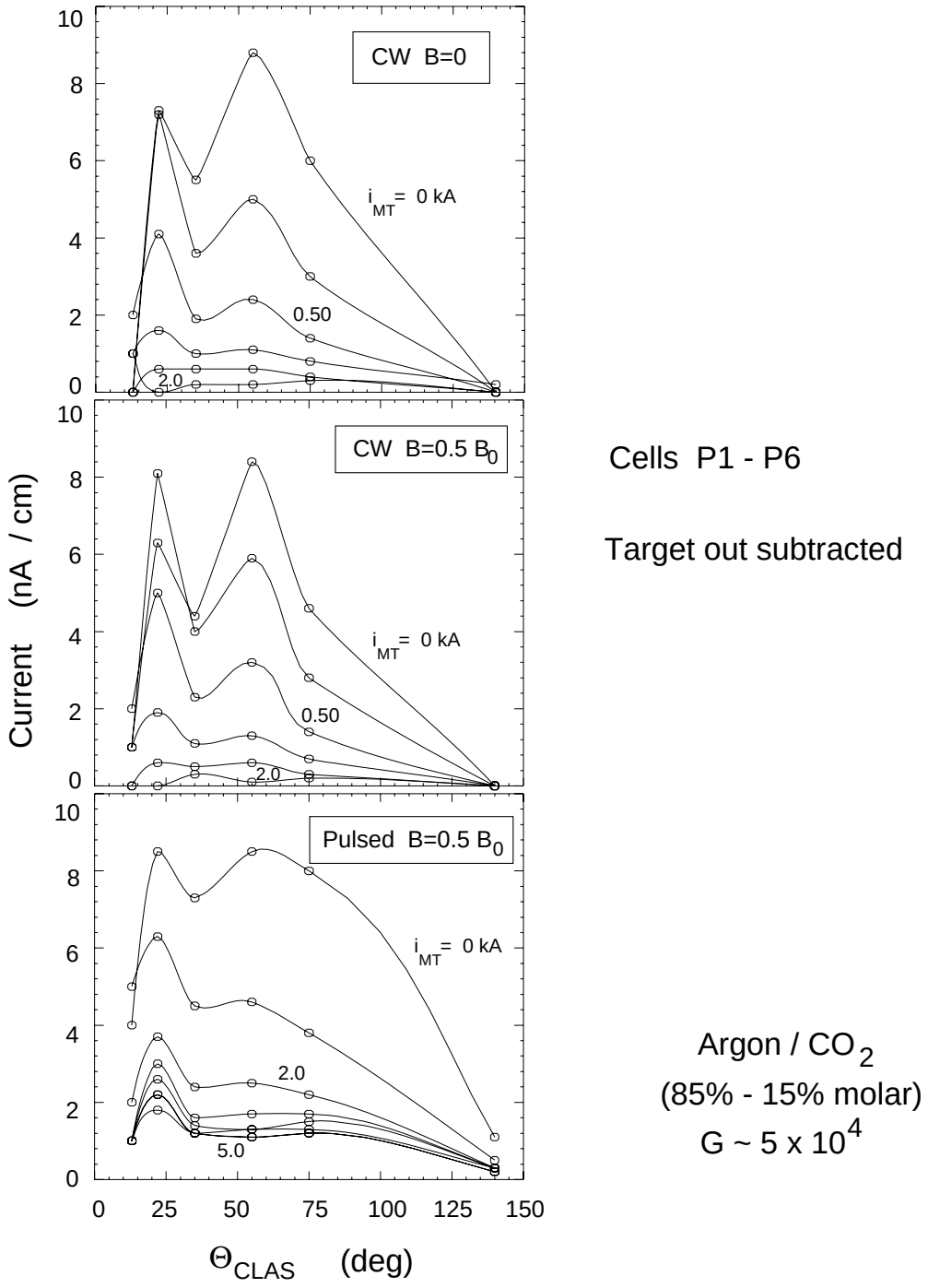

Figure 8: Region I data for the individual drift cells plotting the measured leakage current per centimeter of wire vs. Θ_{CLAS} for a range of minitorus currents. Top: Data with CW beam with main torus field off. Middle: Data with CW beam with main torus at half field. Bottom: Data from pulsed beam with main torus at half field.

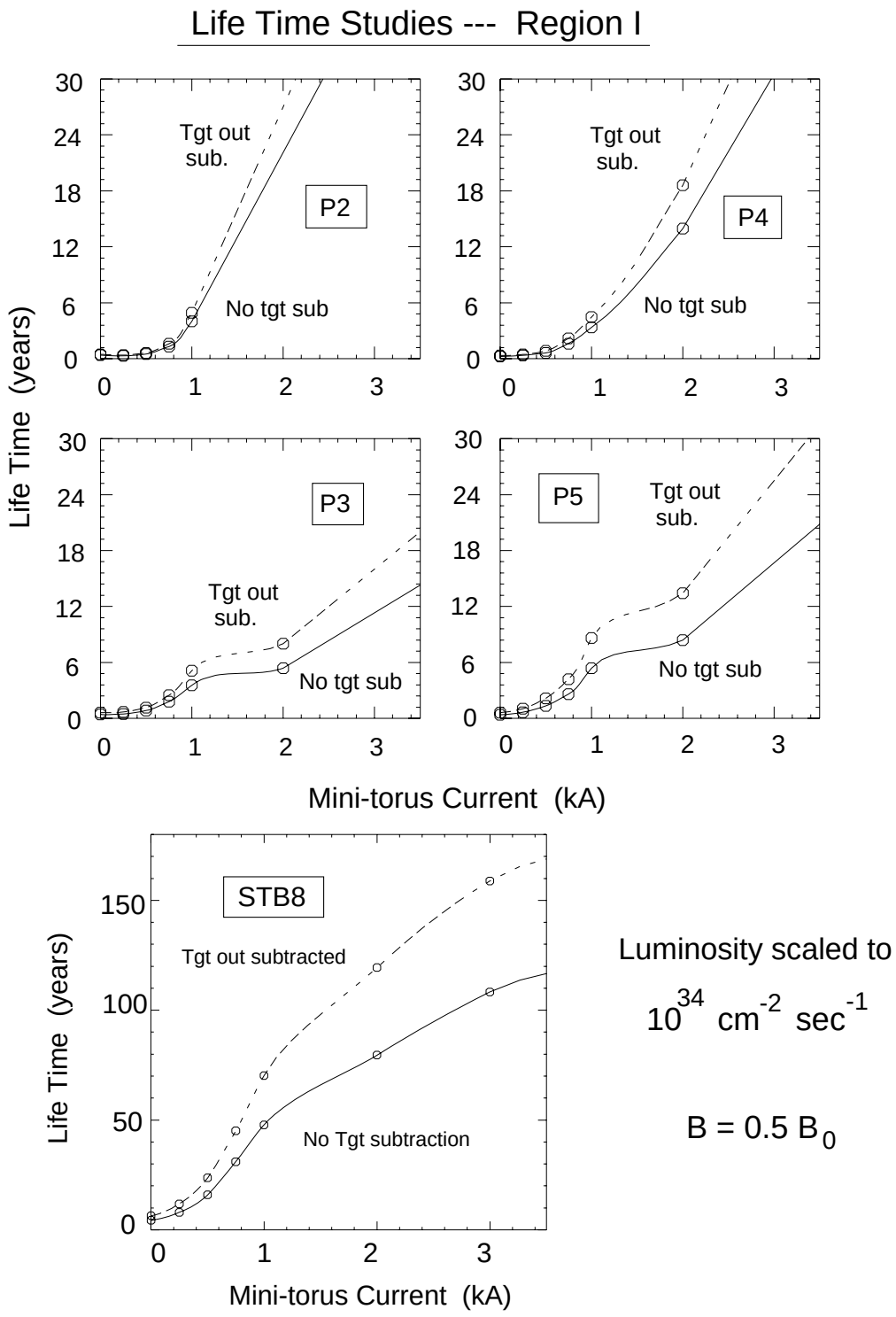

Figure 9: Predicted lifetime for the Region I detector extrapolated from data acquired at a luminosity of 8.4×10^{32} cm^{-2}sec^{-1} to a luminosity of 10^{34} cm^{-2}sec^{-1}. The dashed lines show the lifetime predictions including a subtraction of the target out background currents, while the solid lines show the lifetime predictions without this background subtraction. The lifetime of the chamber is defined for the purposes of this extrapolation to be 1 coulomb of charge acquired per centimeter of wire.

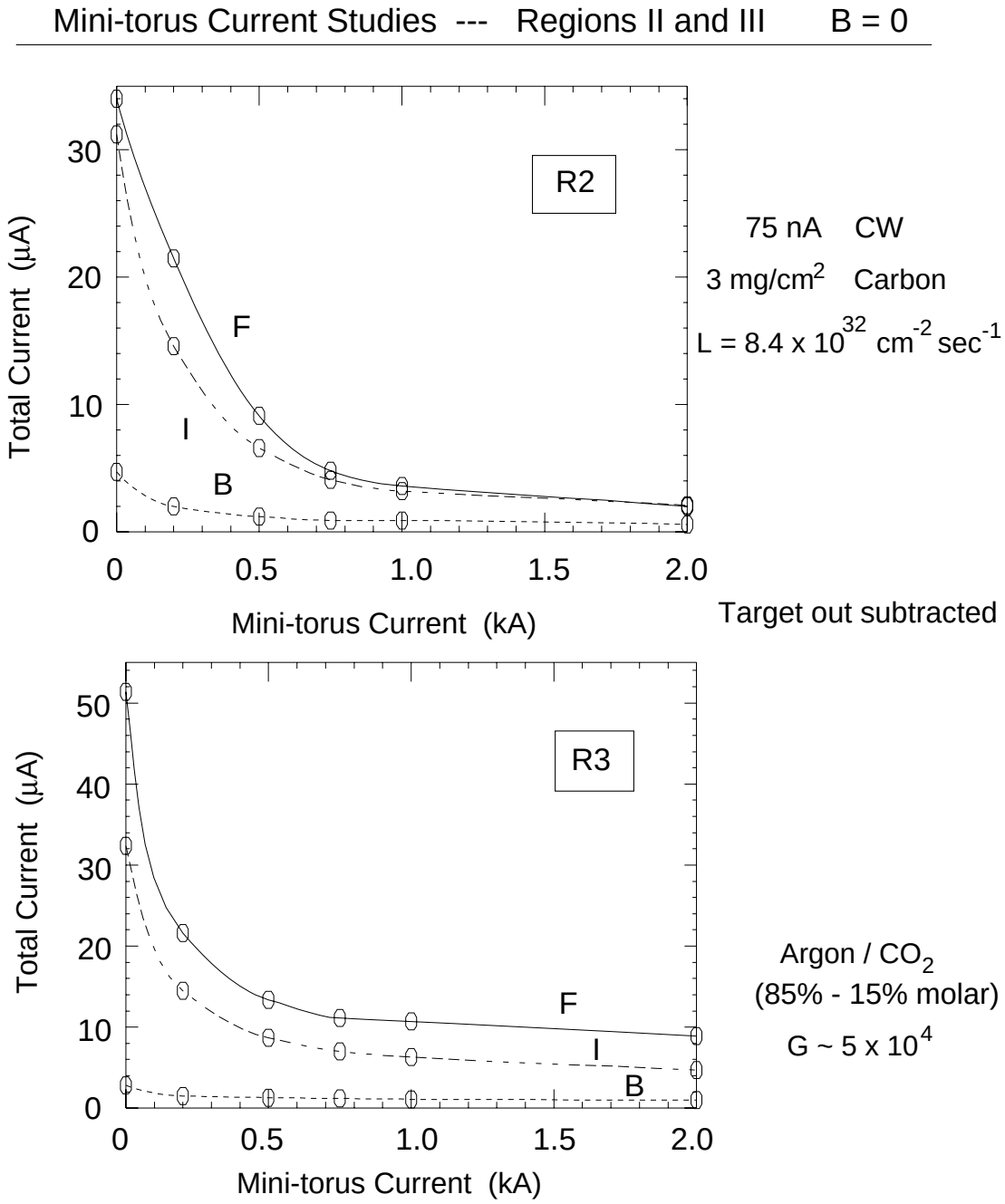

Figure 10: Region II and Region III data plotting the total measured leakage current as a function of minitorus current from 0 to 2 kA. The data show the measured current for the forward, intermediate, and backwards portion of each detector. This data was acquired with a 75 nA CW electron beam on a 3 mg/cm^2 carbon target with the main torus off. The gas mixture and operating conditions of the chambers can be found in the text.

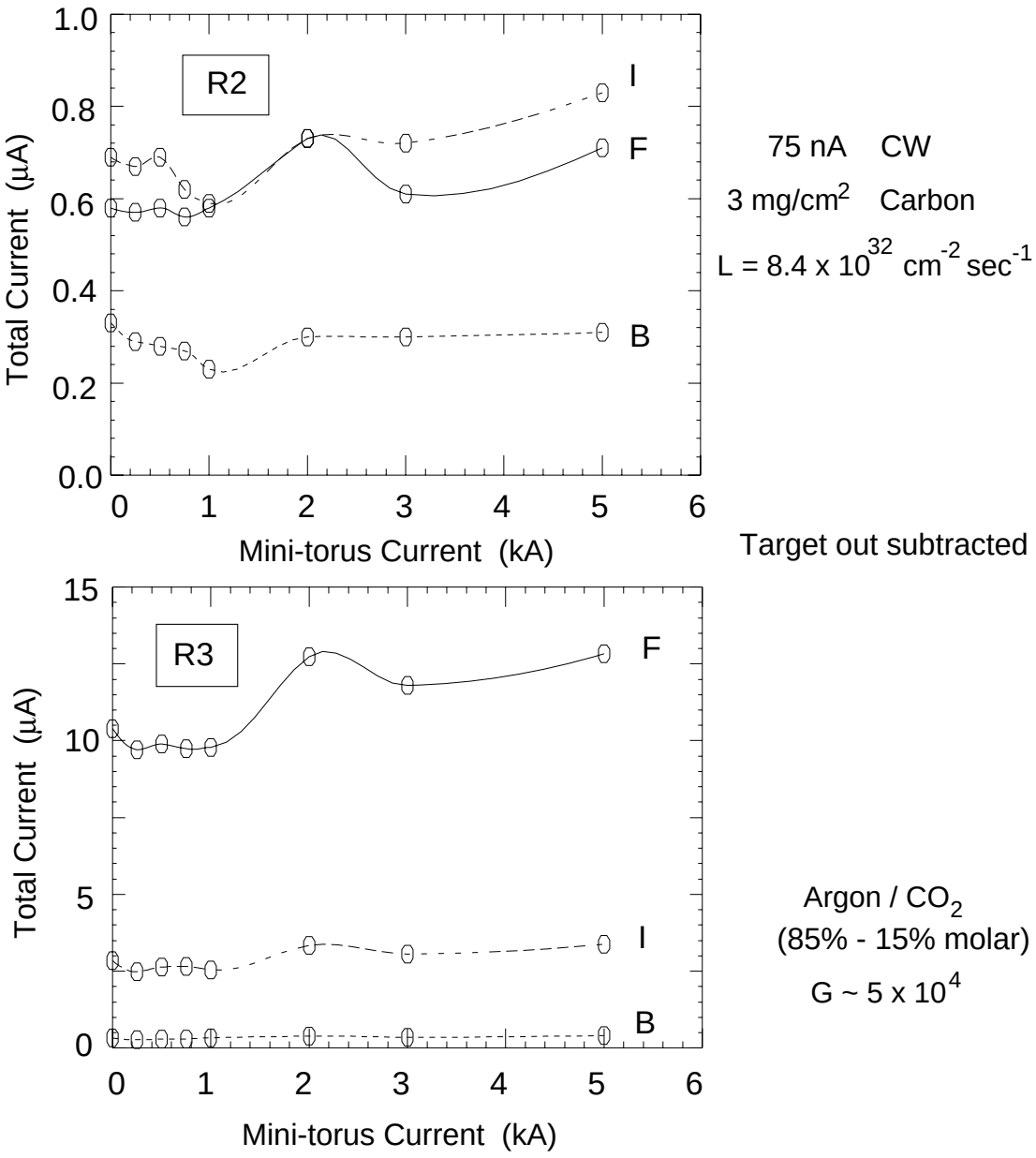

Figure 11: Region II and Region III data plotting the total measured leakage current as a function of minitorus current from 0 to 2 kA. The data show the measured current for the forward, intermediate, and backwards portion of each detector. This data was acquired with a 75 nA CW electron beam on a 3 mg/cm^2 carbon target with the main torus on at half field. The gas mixture and operating conditions of the chambers can be found in the text.